INTERNATIONAL JOURNAL FOR NUMERICAL METHODS IN FLUIDS
Int. J. Numer. Meth. Fluids 2008; **57**:417–436
Published online 8 November 2007 in Wiley InterScience (www.interscience.wiley.com). DOI: 10.1002/fld.1643

Drag prediction, decomposition and visualization in unstructured mesh CFD solver of TAS-code

Wataru Yamazaki*,†,‡, Kisa Matsushima and Kazuhiro Nakahashi

Department of Aerospace Engineering, Tohoku University, Aramaki-Aza-Aoba 6-6-01, Aoba-Ward, Sendai 980-8579, Japan

SUMMARY

The accuracy of drag prediction in unstructured mesh CFD solver of TAS (Tohoku University Aerodynamic Simulation) code is discussed using a drag decomposition method. The drag decomposition method decomposes total drag into wave, profile, induced and spurious drag components, the latter resulting from numerical diffusion and errors. The mesh resolution analysis is conducted by the drag decomposition method. The effect of an advanced unstructured mesh scheme of U-MUSCL reconstruction is also investigated by the drag decomposition method. The computational results show that the drag decomposition method reliably predicts drag and is capable of meaningful drag decomposition. The accuracy of drag prediction is increased by eliminating the spurious drag component from the total drag. It is also confirmed that the physical drag components are almost independent of the mesh resolution and scheme modification.

Received 19 February 2007; Revised 12 September 2007; Accepted 18 September 2007

KEY WORDS: unstructured mesh CFD; drag prediction and decomposition; TAS-code; spurious drag; mesh resolution; U-MUSCL

1. INTRODUCTION

The lift and drag of an aircraft in the cruising condition are known to be the most important parameters affecting the aerodynamic performance. Recently, owing to advances in numerical schemes and the rapid growth of computing power, computational fluid dynamics (CFD) has achieved significant progress. However, the accurate drag prediction in CFD is still one of the major challenges and crucial issues in the field of aerospace engineering, as was pointed out at the

*Correspondence to: Wataru Yamazaki, Department of Aerospace Engineering, Tohoku University, Aramaki-Aza-Aoba 6-6-01, Aoba-Ward, Sendai 980-8579, Japan.
†E-mail: yamazaki@ad.mech.tohoku.ac.jp
‡Postdoctoral Researcher, DAAP, ONERA.

Contract/grant sponsor: Japan Society for the Promotion of Science

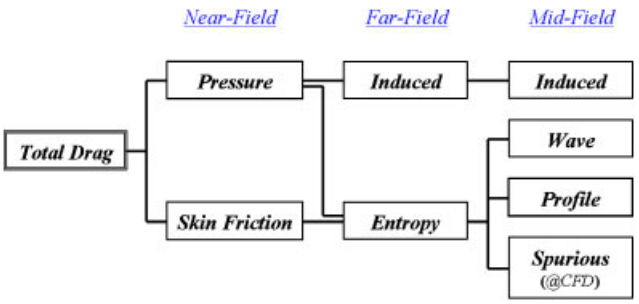

Figure 1. Drag components and the classification.

meeting of AIAA Drag Prediction Workshop (DPW) [1–5]. In fact, the drag prediction accuracy within 1 drag count (1×10^{-4}, about 0.4% in total drag of a typical transonic aircraft) has still not been achieved. The two major error sources are pointed out, one is the turbulence/transition modeling and the other is the numerical diffusion due to discretization and insufficient mesh resolution. Especially in CFD approaches using unstructured meshes, they tend to suffer from more numerical diffusion than that in structured meshes, which results in the inaccuracy of drag prediction. This issue may occur because of the lower spatial accuracy and occasional larger mesh distortion of unstructured meshes. Therefore, accurate drag prediction by the elimination of the effect of numerical diffusion is essential for the practical use of the unstructured mesh CFD.

Traditionally, surface integration of the pressure and stress tensor on the surface of the aircraft body, which is called 'surface integration' or 'near-field method', is used for drag prediction in CFD computations. However, it has been pointed out that the total drag computed by the near-field method includes inaccuracies relating to numerical diffusion and errors and that such inaccuracies cannot be isolated from the total drag.

Recently, two advanced drag prediction methods based on the theory of momentum conservation around an aircraft have attracted much attention. One is called 'wake integration' or 'far-field method' [6–8] which can compute drag components from surface integration on the wake plane downstream of the aircraft. The other is called 'flow-field integration' or 'mid-field method' [9–14], which can compute drag components from volume integration around the aircraft, and is derived from the far-field method by applying the divergence theorem, also known as Gauss' theorem. In the mid-field method, the spurious drag component, which is due to the effect of spurious entropy production based on numerical diffusion, can be computed and isolated from the total drag; this should enable more accurate drag prediction.

Other advantages of the mid-field method are that it enables the drag to be decomposed and visualized. By using the mid-field method, the total drag can be decomposed into three physical components of wave, profile and induced drag, and one spurious drag component. In Figure 1, these drag components and the classification are summarized. (Note that, in this paper, profile drag is defined as a drag component based on the entropy production due to the effect of the boundary layer and wake.) Moreover, the drag amount and the generated positions can be visualized in the flow field because the integrand of the volume integral formula indicates the drag production rate per unit volume. Recently, aerodynamic shape design and optimizations using CFD are widely conducted, and these require detailed analyses of the drag reduction level, mechanisms and reliability. The ability to decompose and visualize drag would be most useful for such investigations [14].

DOI: 10.1002/fld

In this paper, the mid-field drag decomposition method is therefore applied to unstructured mesh CFD results of TAS-code and its capability is analyzed.

2. DRAG DECOMPOSITION METHODS

This section outlines the concept and computational method of the three drag prediction methods.

2.1. Near-field method

In the near-field method, the drag force is computed as follows:

$$D = \iint_{\text{Body}} [-(P - P_\infty)n_x + \boldsymbol{\tau}_x \cdot \mathbf{n}]\, \mathrm{d}s \tag{1}$$

The integral area 'Body' indicates the surface of the aircraft. The first and second terms correspond to the pressure and skin friction drag components, respectively.

2.2. Far-field method

In the drag prediction method based on the theory of momentum conservation, the drag force is computed as follows:

$$D = \iint_{\mathbf{S}_\infty} [-\rho(u_x - u_\infty)(\mathbf{u}\cdot\mathbf{n}) - (P - P_\infty)n_x + \boldsymbol{\tau}_x \cdot \mathbf{n}]\, \mathrm{d}s \tag{2}$$

The integral area '$\mathbf{S}_\infty$' indicates an arbitrary closed surface around the aircraft. It has been demonstrated that Equation (2) can be transformed as follows by using the small perturbation approximation [6]:

$$\begin{aligned} D &= \iint_{\text{WA}} P_\infty \frac{\Delta s}{R}\, \mathrm{d}s - \iint_{\text{WA}} \rho_\infty \Delta H\, \mathrm{d}s + \iint_{\text{WA}} (\mathbf{F}_{\text{ind}} \cdot \mathbf{n})\, \mathrm{d}s + O(\Delta^2) \\ \mathbf{F}_{\text{ind}} &= \left(\frac{\rho_\infty}{2} [(u_y^2 + u_z^2) - (1 - M_\infty^2)(\Delta u_x)^2], -\rho_\infty u_y \Delta u_x, -\rho_\infty u_z \Delta u_x \right) \end{aligned} \tag{3}$$

The integral area 'WA' indicates a wake plane normal to the free stream flow direction, as shown schematically in Figure 2. The first term of Equation (3) corresponds to entropy drag which includes the wave, profile and spurious drag components. The second term including ΔH can be neglected in cases where external work is not supplied in flow. The third term including $\mathbf{F}_{\text{ind}}$ originates in the vorticity, which corresponds to induced drag.

2.3. Mid-field method

As mentioned in the previous section, the mid-field method is derived from the far-field method by applying the divergence theorem, also known as Gauss' theorem. First, the concept is explained using the entropy and enthalpy term. By using the divergence theorem, the entropy and enthalpy term of the far-field method can be transformed as follows [9]:

$$D_{(\Delta s, \Delta H)} = \iint_{\text{WA}} \mathbf{F}_{(\Delta s, \Delta H)} \cdot \mathbf{n}\, \mathrm{d}s \cong \iint_{\mathbf{S}_\infty} \mathbf{F}_{(\Delta s, \Delta H)} \cdot \mathbf{n}\, \mathrm{d}s = \iiint_{\mathbf{V}} \nabla \cdot \mathbf{F}_{(\Delta s, \Delta H)}\, \mathrm{d}v \tag{4}$$

DOI: 10.1002/fld

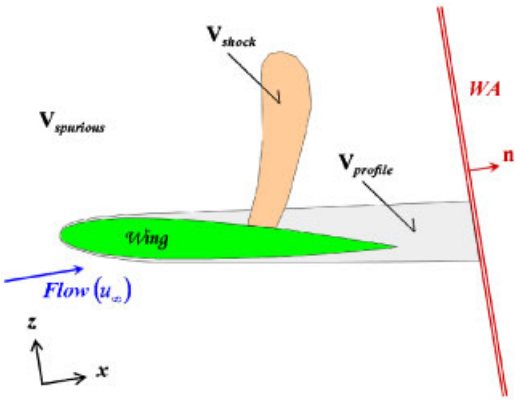

Figure 2. Schematic sketch for far- and mid-field method.

where $\mathbf{V}$ indicates the flow field around the aircraft; hence $\mathbf{S}_\infty$ indicates the closed boundary surface of $\mathbf{V}$. In other words, $\mathbf{S}_\infty$ consists of the wake plane of 'WA' and the far-field surfaces of the upstream/lateral regions. $\mathbf{F}_{(\Delta s,\Delta H)}$ is the entropy and enthalpy drag vector, which is defined as follows [9]:

$$\begin{aligned}\mathbf{F}_{(\Delta s,\Delta H)} &= -\rho\Delta\overline{u}\mathbf{u}\\ \Delta\overline{u} &= u_\infty\sqrt{1+\frac{2\Delta H}{u_\infty^2}-\frac{2[e^{((\gamma-1)/\gamma)(\Delta s/R)}-1]}{(\gamma-1)M_\infty^2}}-u_\infty\end{aligned} \tag{5}$$

$\Delta\overline{u}$ of Equation (5) can be expanded in Taylor's series with respect to the entropy variation and stagnation enthalpy variation as follows:

$$\begin{aligned}\Delta\overline{u}/u_\infty = {} & f_{s1}(\Delta s/R)+f_{s2}(\Delta s/R)^2+f_{H1}(\Delta H/u_\infty^2)+f_{H2}(\Delta H/u_\infty^2)^2\\ & +f_{sH2}(\Delta s/R)(\Delta H/u_\infty^2)+O(\Delta^3)\end{aligned} \tag{6}$$

Here,

$$f_{s1}=-\frac{1}{\gamma M_\infty^2},\quad f_{s2}=-\frac{1+(\gamma-1)M_\infty^2}{2\gamma^2M_\infty^4},\quad f_{H1}=1,\quad f_{H2}=-\frac{1}{2},\quad f_{sH2}=\frac{1}{\gamma M_\infty^2} \tag{7}$$

Now, calculate the first-order term of entropy variation as follows:

$$\mathbf{F}_{\Delta s1}=\frac{u_\infty}{\gamma M_\infty^2}\frac{\Delta s}{R}\rho\mathbf{u} \tag{8}$$

Equation (8) is the well-known Oswatitsch formula itself. Substituting Equation (8) into Equation (4), the first-order entropy drag term can be rewritten as follows:

$$D_{\text{Entropy}}=\iint_{\mathbf{S}_\infty}\frac{P_\infty}{\rho_\infty u_\infty}\frac{\Delta s}{R}(\rho_\infty+\Delta\rho)(\mathbf{u}_\infty+\Delta\mathbf{u})\mathbf{n}\,\mathrm{d}s\cong\iint_{\text{WA}}P_\infty\frac{\Delta s}{R}\,\mathrm{d}s \tag{9}$$

DOI: 10.1002/fld

Here, the small perturbation approximation and formulation $a_\infty^2 = \gamma P_\infty / \rho_\infty$ were used. It can be confirmed that Equation (9) is the first term of Equation (3) itself.

By the transformation to the volume integral form, further drag decomposition of the entropy drag term is possible by the domain decomposition of the flow field $\mathbf{V}$. Physically, entropy variation in the flow field should originate in the shock ($\mathbf{V}_{\text{shock}}$) and wake/boundary layer regions ($\mathbf{V}_{\text{profile}}$); hence, the entropy variation in the remaining region ($\mathbf{V}_{\text{spurious}}$) is considered to be an unphysical (spurious) phenomenon. The domain decomposition of the flow field is schematically shown in Figure 2. Then Equation (4) can be transformed as follows:

$$D_{(\Delta s,\Delta H)} = \iiint_{\mathbf{V}_{\text{shock}}} \nabla \cdot \mathbf{F}_{(\Delta s,\Delta H)}\, \mathrm{d}v + \iiint_{\mathbf{V}_{\text{profile}}} \nabla \cdot \mathbf{F}_{(\Delta s,\Delta H)}\, \mathrm{d}v + \iiint_{\mathbf{V}_{\text{spurious}}} \nabla \cdot \mathbf{F}_{(\Delta s,\Delta H)}\, \mathrm{d}v$$
$$= D_{\text{wave}} + D_{\text{profile}} + D_{\text{spurious}} \tag{10}$$

where D_{wave}, D_{profile} and D_{spurious} correspond to wave, profile and spurious drag components, respectively. Moreover, we can evaluate each drag component like a flux computation using the divergence theorem again as follows (only the formula for wave drag is described):

$$D_{\text{wave}} = \iiint_{\mathbf{V}_{\text{shock}}} \nabla \cdot \mathbf{F}_{(\Delta s,\Delta H)}\, \mathrm{d}v = \iint_{\mathbf{S}_{\text{shock}}} \mathbf{F}_{(\Delta s,\Delta H)} \cdot \mathbf{n}\, \mathrm{d}s \tag{11}$$

where $\mathbf{S}_{\text{shock}}$ indicates the boundary surface of $\mathbf{V}_{\text{shock}}$. As the reader can guess, the spurious entropy drag may be generated in the shock and profile regions, and the effect cannot be isolated in this approach. However, it is known that the majority of the spurious drag is generated in a region around the leading edge which is outside of the profile (boundary layer) region. Hence, the spurious drag generated in the shock and profile regions is insignificant. This insignificance will be discussed later. The advantages of the mid-field method are that it can divide the entropy drag into the wave, profile and spurious drag components and can visualize the generated positions and the drag amount in the flow field because the integrand of the volume integral form indicates the drag production rate per unit volume.

The domain decomposition of flow field is conducted based on the following shock and profile detective functions. For the detection of the shock region, the following function is used [15]:

$$f_{\text{shock}} = (\mathbf{u} \cdot \nabla P)/(a|\nabla P|) \tag{12}$$

For the detection of the wake and boundary layer regions, the following function is used [11]:

$$f_{\text{profile}} = (\mu_{\text{l}} + \mu_t)/(\mu_{\text{l}}) \tag{13}$$

The regions that satisfy $f_{\text{shock}} \geqslant 1$ and $f_{\text{profile}} \geqslant C_{\text{pro}} \cdot (f_{\text{profile}})_\infty$ are recognized as the upstream region of shock waves and the profile region, respectively. C_{pro} is a cutoff value for selecting the profile region. In Section 4.1, the insensitivity of C_{pro} is validated and $C_{\text{pro}} = 1.1$ is used in this research.

Similarly, the induced drag can be evaluated as follows:

$$D_{\text{induced}} = \iint_{\text{WA}} \mathbf{F}_{\text{ind}} \cdot \mathbf{n}\, \mathrm{d}s \cong \iint_{\mathbf{S}_\infty} \mathbf{F}_{\text{ind}} \cdot \mathbf{n}\, \mathrm{d}s \tag{14}$$

In the computational execution, the drag fluxes on an edge are evaluated by the arithmetic mean from the node points of both ends. For the entropy drag, the contribution of each edge which is

DOI: 10.1002/fld

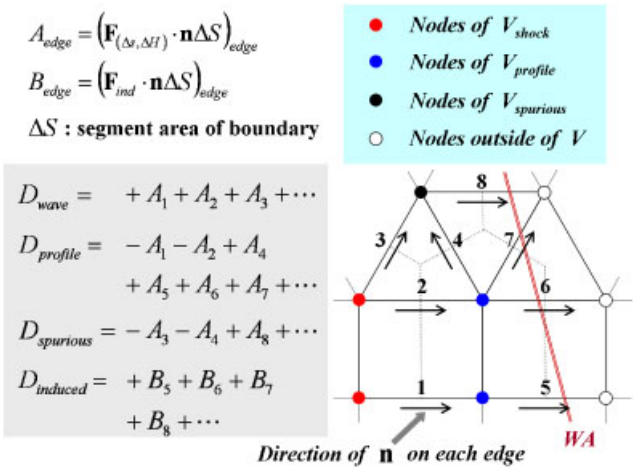

Figure 3. Schematic sketch for mid-field drag computation.

located at the domain boundary of $\mathbf{V}_{\text{shock}}$, $\mathbf{V}_{\text{profile}}$ and $\mathbf{V}_{\text{spurious}}$ is summing up to each component. For the induced drag, the contribution of each edge which is located at the boundary of $\mathbf{V}$ is summing up. This algorithm is schematically shown in Figure 3.

3. FLOW SOLVER

For flow computations, three-dimensional flows were analyzed using the TAS (Tohoku University Aerodynamic Simulation)-code [16]. Compressible Reynolds-averaged Navier–Stokes equations were solved by a finite-volume cell-vertex scheme on an unstructured hybrid mesh. The numerical flux normal to the control volume boundary was computed using an approximate Riemann solver of Harten–Lax–van Leer–Einfelds–Wada (HLLEW) [17]. The Lower–Upper Symmetric Gauss–Seidel (LU-SGS) implicit method for unstructured meshes [18] was used for the time integration. The original Spalart–Allmaras model [19] was adopted to treat turbulent boundary layers, and fully turbulent flow was assumed in the computation.

In the TAS-code, the second-order spatial accuracy is achieved by a conventional linear reconstruction of the primitive gas dynamic variables inside the control volume with Venkatakrishnan's limiter [20] as follows:

$$Q_{ij}^{\mathrm{L}} = Q_i + \Psi_i \left(\nabla Q_i \cdot \frac{\mathbf{r}_{ij}}{2} \right) \tag{15}$$

where Q_{ij}^{L} is an extrapolated variable from the left side to the face between nodes i and j as shown in Figure 4. Recently, a more accurate method for the variable extrapolation, unstructured MUSCL (U-MUSCL) [21], has been suggested. In this method, using the variable of the neighboring node Q_j, more accurate extrapolation is realized as follows:

$$Q_{ij}^{\mathrm{L}} = Q_i + \Psi_i \left(\frac{\kappa}{2}(Q_j - Q_i) + (1-\kappa)\nabla Q_i \cdot \frac{\mathbf{r}_{ij}}{2} \right) \tag{16}$$

DOI: 10.1002/fld

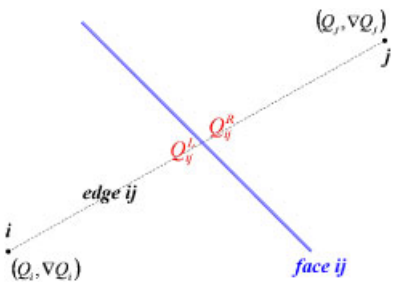

Figure 4. Schematic sketch for U-MUSCL extrapolation.

where κ is a U-MUSCL parameter. If κ is set to 0, the conventional extrapolation formula, Equation (15), is obtained. If κ is set to 1, the extrapolated variable can be obtained as the arithmetic mean of Q_i and Q_j (assuming no limiter). In this case, the scheme has the characteristics of the central difference scheme and becomes unstable. The third-order extrapolation (note: not third-order accuracy) can be achieved by setting κ to 0.5. The details of the U-MUSCL are given in [21]. In Section 4.3, the effectiveness of the U-MUSCL scheme is discussed using the mid-field drag decomposition method. The conventional reconstruction method of Equation (15) is used in Sections 4.1 and 4.2. All computations executed in this paper were fully converged within the order of 0.1 drag count.

4. RESULTS AND DISCUSSION

4.1. Validation study in ONERA M6 transonic computation

In this section, the validation study of the drag decomposition method is conducted using the ONERA M6 transonic computation. The polar curve was computed at a Mach number of 0.84. The number of mesh points was 2.3 million. The unstructured hybrid mesh was generated using the TAS-mesh package, which includes the surface mesh generation using an advancing front approach [22], tetrahedral volume mesh generation using a Delaunay approach [23] and hybrid mesh generation using an advancing layer approach [24]. The number of prism layers was set to 35. In Figures 5 and 6, the shock visualization using Equation (12) and 65% semi-span's C_p distribution with experimental data [25] at the angle of attack of 3.06° is shown. The maximum $y+$ value was about 1.5 in this computation.

In order to predict the induced drag component, the diffusion of the wingtip vortex has to be considered. The wingtip vortex diffuses and transforms into entropy generation equivalently in the wake region. Hence, the entropy drag term obtained by integrating from the wingtip to the downstream boundary surface WA has to be considered as an additional term for the induced drag component. In Figure 7, the variation of each drag component with the expansion of the integral region (the movement of WA) to the downstream direction is shown. The position of the trailing edge at the wingtip corresponds to the WA of 1.4. In this figure, the prefixes *NF_* and *MF_* represent the near-field and mid-field drag predictions, respectively. With the movement to the downstream direction, the 'original' induced drag term (*MF_Induced**) was reduced and the 'additional' induced drag term (*Wake's Entropy Drag*) was increased. The sum of the original and

DOI: 10.1002/fld

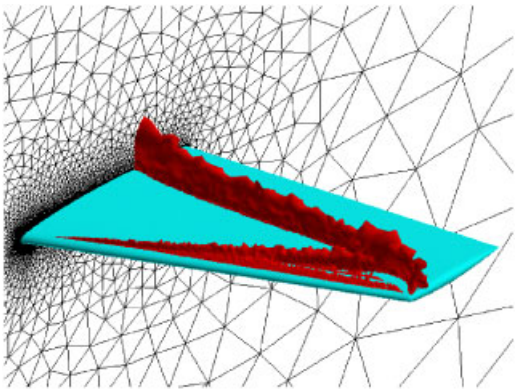

Figure 5. Shock visualization of ONERA M6 wing.

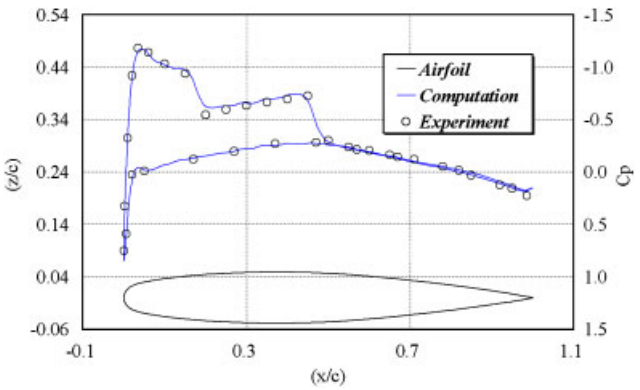

Figure 6. C_p distribution of ONERA M6 wing at 65% semi-span.

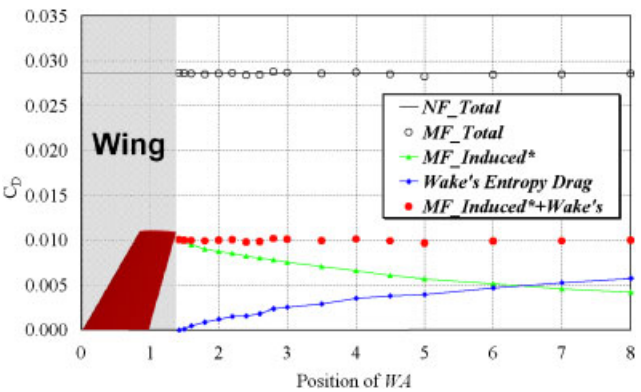

Figure 7. Induced drag prediction in wake region.

DOI: 10.1002/fld

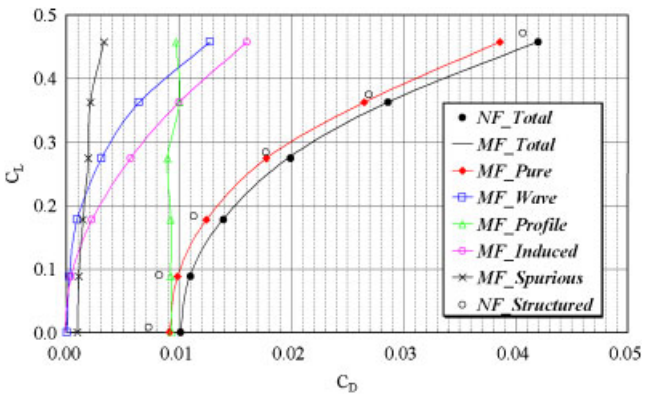

Figure 8. Drag polar of ONERA M6 wing at Mach 0.84.

additional terms was almost constant at arbitrary positions of WA, meaning that the 'total' induced drag was almost conserved in the wake region. Then, it was confirmed that the mid-field total drag (*MF_Total*) showed good agreement with the near-field total drag (*NF_Total*) at arbitrary positions of WA.

The drag decomposition result of the drag polar computations is shown in Figure 8. In this figure, a structured mesh near-field result [13] is also plotted (*NF_Structured*). The Baldwin–Lomax turbulence model was adopted in this structured mesh computations, and the number of mesh points was almost same as that of the unstructured one. It was confirmed in all the computations that the total drag computed by the mid-field method showed good agreement with that computed by the near-field method. In detail, the wave drag and induced drag were found to increase with higher angle of attack. The profile drag increased slightly at high-lift conditions, which was the effect of separation. The *MF_Pure* plot is defined as 'pure' drag and indicates the sum of the physical drag components, in other words, the remainder after subtracting the spurious drag from the total drag. The pure drag showed better agreement with the structured mesh result compared with the total drag. This meant that more accurate drag prediction was achieved by using the drag decomposition method.

The parametric study of C_{pro}, in other words, the sensitivity analysis of the detective sensor of the profile region, was also conducted. In Figure 9, the results of the pure/profile drag prediction are shown for the cases of $C_{\text{pro}} = 1.1$, 1.5 and 2.0. It was confirmed that the pure and profile drag were almost insensitive to the parameter C_{pro}. The domain decomposition results at $C_{\text{pro}} = 1.1$ and 2.0 are shown in Figure 10. It is obvious that the domain decomposition results are almost insensitive to the variation of C_{pro}. This result showed that the parameter C_{pro} had the independency of the mid-field drag prediction and decomposition.

The visualization of mesh, pressure, entropy variation and entropy drag distribution $\nabla \cdot \mathbf{F}_{(\Delta s, \Delta H)}$ at an angle of attack of 3.06°, 65% semi-span section is included in Figure 10. The production of entropy drag at the leading/trailing edge, boundary layer, shock positions and wake region was confirmed. The spurious drag was mainly generated around the leading edge and was caused by the numerical diffusion relating to the mesh coarseness against the rapid change in the flow variables. The entropy drag production around the trailing edge was considered to be the effect of the wake's massive diffusion.

DOI: 10.1002/fld

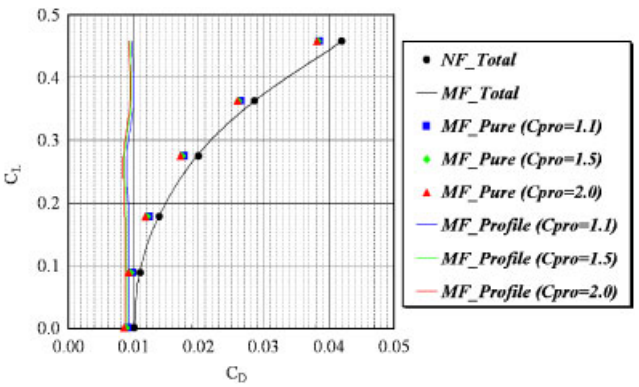

Figure 9. Sensitivity analysis of C_{pro}.

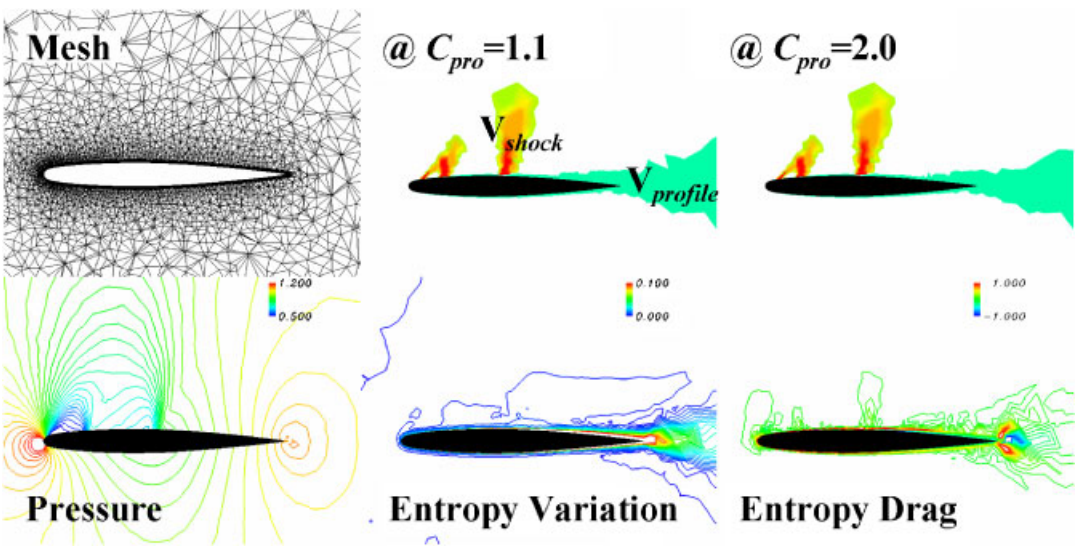

Figure 10. Flow-field visualization of ONERA M6 Wing at 65% semi-span.

4.2. Mesh resolution analysis in DPW-2 problem

In this section, the mesh resolution effect is analyzed using the DLR-F6 wing-body configuration. The geometry, flow conditions and so on were the same as used in the second AIAA Drag Prediction Workshop [1] held in 2003. In this analysis, the three computational meshes provided as the official unstructured meshes for DPW-2 were used. The numbers of mesh points were 1, 3 and 9 millions, respectively. The number of prism layers was from 26 to 33 in all meshes. The details of the mesh generation methods are given in [26]. In this section, the 1, 3 and 9 millions meshes are called 'coarse', 'medium' and 'fine' mesh, respectively. These meshes are visualized in Figure 11. The polar curve was computed at a Mach number of 0.75. For the fine mesh, only one case at an angle of attack of 0.49° was conducted. In all cases, $y+$ was less than one over

DOI: 10.1002/fld

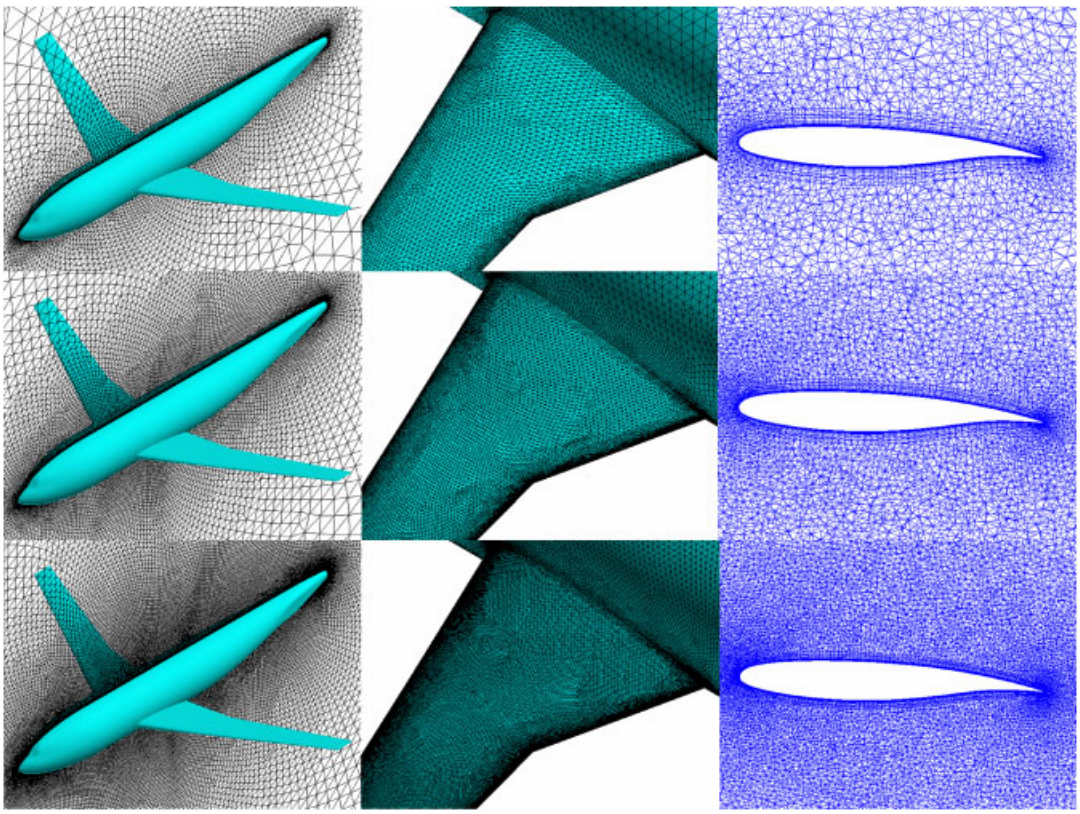

Figure 11. Computational mesh visualization of DLR-F6 wing-body configuration, from upper to lower: coarse, medium and fine meshes.

most of the airplane surface. The maximum $y+$ values of the coarse, medium and fine meshes at the angle of attack of 0.49° were about 3.2, 2.2 and 1.6, respectively.

In Figures 12 and 13, the comparison of C_p distributions at an angle of attack of 0.49°, 33% semi-span section and the drag prediction results using the near-field method are shown with the experimental data [1]. Although more detailed analyses for the turbulent model and/or transition are required to compare the computational results and the experimental data quantitatively, it was confirmed from Figure 12 that the C_p distributions of all computations showed good agreement with the experimental data qualitatively. In Figure 13, the structured mesh result of the elsA code provided at DPW-2 [4] is also included. The k–ω turbulence model suggested by Wilcox was adopted in this structured mesh computations, and the mesh resolution was almost same with that of the unstructured medium mesh. The total drag was reduced with the increase in the mesh resolution, and the medium and fine meshes showed good agreement with the experimental data. On the other hand, the total drag of the coarse mesh showed a difference of about 30 cts while the skin friction drag showed good agreement with the medium mesh. This implied that the spurious drag in the pressure drag component was reduced with the increase in the mesh resolution.

In Figure 14, the drag decomposition results of the three meshes at an angle of attack of 0.49° are compared. The physical drag components—wave, profile and induced drag—showed good

DOI: 10.1002/fld

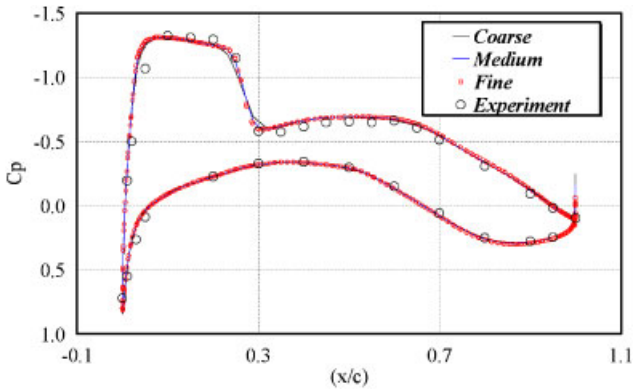

Figure 12. C_p distribution of DLR-F6 wing-body configuration at 33% semi-span.

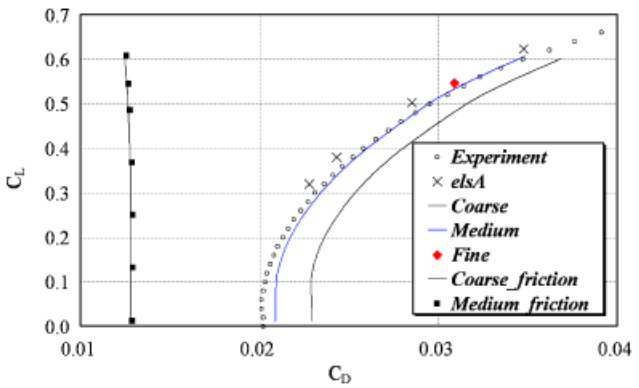

Figure 13. Near-field drag prediction of DLR-F6 wing-body configuration at Mach 0.75.

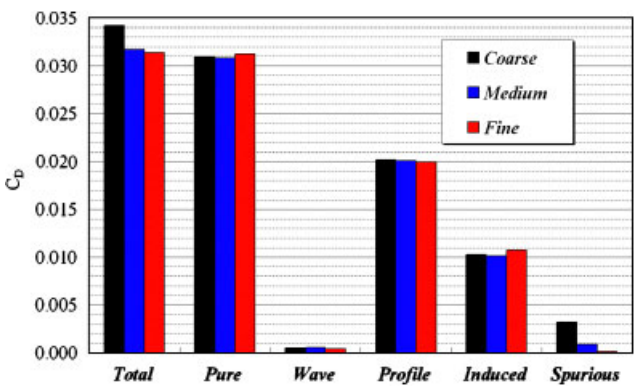

Figure 14. Comparison of drag components of DLR-F6 wing-body configuration.

DOI: 10.1002/fld

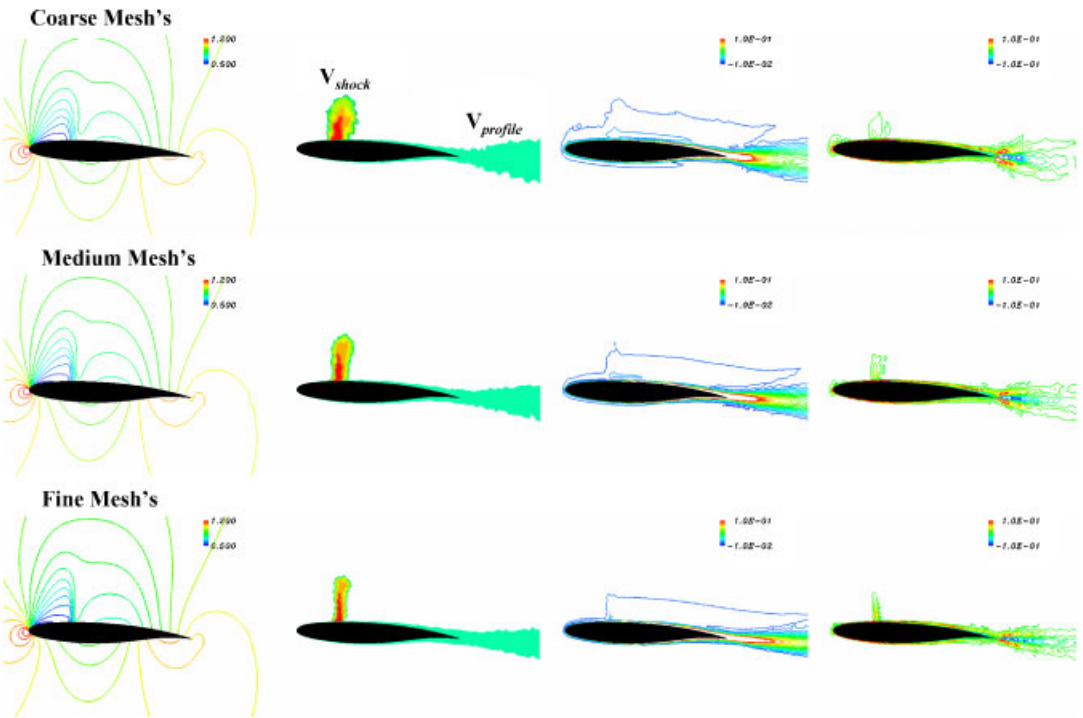

Figure 15. Flow-field visualization of DLR-F6 wing-body configuration at 33% semi-span, from left to right: pressure, domain decomposition, entropy variation and entropy drag distribution.

agreement between the three results while the spurious drag was reduced with the increase in the mesh resolution. This meant that the physical drag components could be predicted almost independent of the mesh resolution by using the drag decomposition method. In addition, this result implied that the spurious entropy drag existing in the shock/profile regions was much smaller than that of the spurious region since the wave/profile drag components were almost constant in all three meshes. In Figure 15, the flow-field visualizations at an angle of attack of 0.49°, 33% semi-span section are shown. It was confirmed that the spurious entropy (and spurious entropy drag) production around the leading edge and the wake's diffusion were reduced with the increase in the mesh resolution. In Figure 16, the entropy drag production maps on the x–y plane are shown. To create this figure, first a uniform Cartesian mesh was made on the x–y plane, then the entropy drag amount $(\nabla \cdot \mathbf{F}_{(\Delta s, \Delta H)}\, \mathrm{d}v)$ of each node of unstructured mesh was integrated to each cell of the Cartesian mesh referring to the x–y coordinates as shown in Figure 17. The red/blue points at the left side indicate the diffusion of wingtip vortex and wake. From Figure 16, the reduction of (spurious) entropy drag around the nose of fuselage and leading/trailing edge was confirmed with the increase in the mesh resolution.

In Figure 18, the drag decomposition results of the coarse and medium meshes are shown with the result of elsA code [4]. The physical drag components showed good agreement between them. On the other hand, the spurious drag component was reduced from about 30 to 10 cts with the

DOI: 10.1002/fld

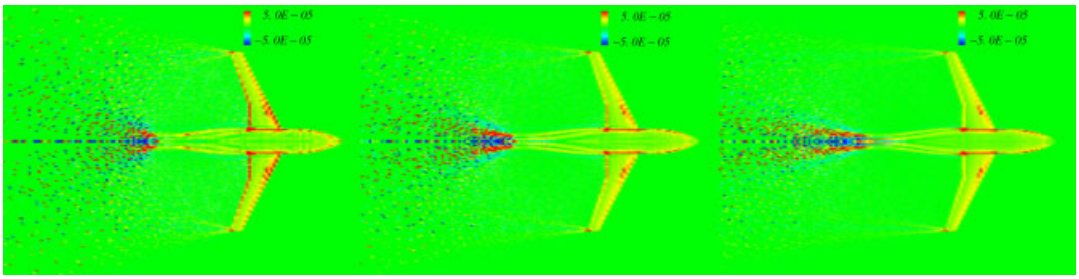

Figure 16. Entropy drag production map, from left to right: coarse, medium and fine meshes results.

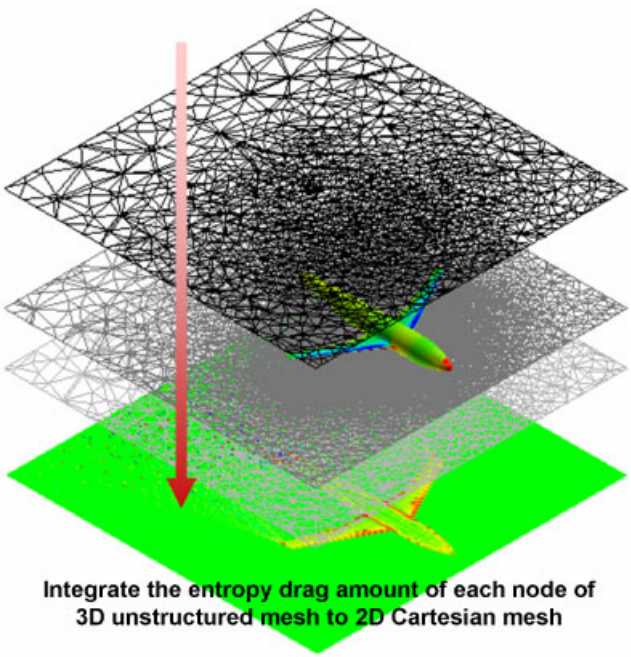

Figure 17. How to make entropy drag production map.

increase in the mesh resolution. In Figure 19, the pure drag is plotted with the near-field results and the experimental data. The pure drag of the coarse and medium meshes showed much better agreement with the experimental data than the near-field drag prediction.

4.3. U-MUSCL scheme analysis

In this section, the effectiveness of the U-MUSCL scheme is analyzed using the DLR-F6 transonic computation. The flow conditions were a Mach number of 0.75 and angle of attack of 0.49°. The coarse computational mesh introduced in the previous section was used for the analysis.

DOI: 10.1002/fld

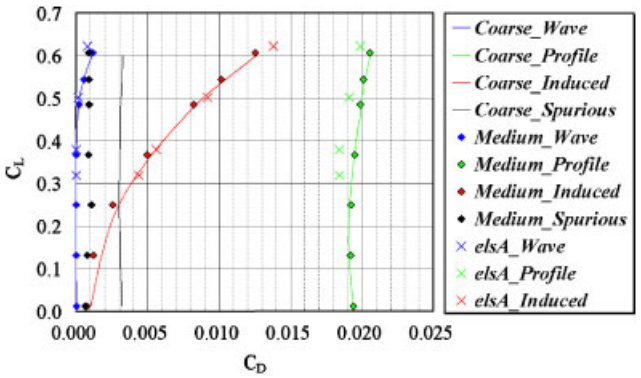

Figure 18. Drag decomposition results of DLR-F6 wing-body configuration.

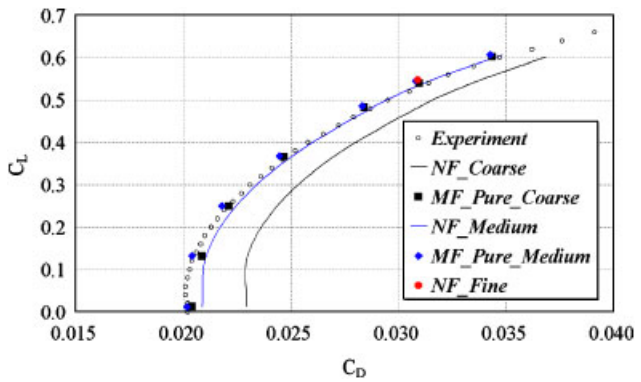

Figure 19. Pure drag prediction of DLR-F6 wing-body configuration.

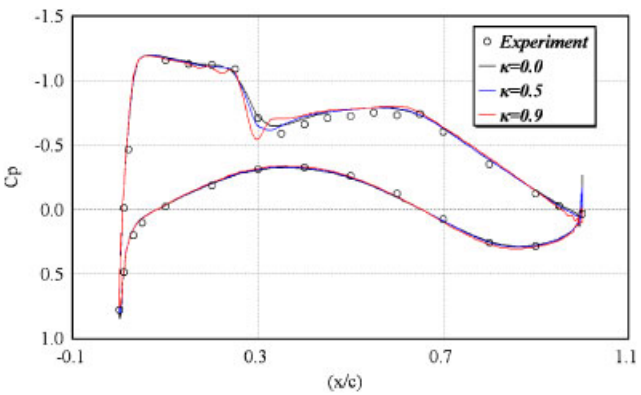

Figure 20. C_p distribution at 41% semi-span for U-MUSCL scheme analysis.

DOI: 10.1002/fld

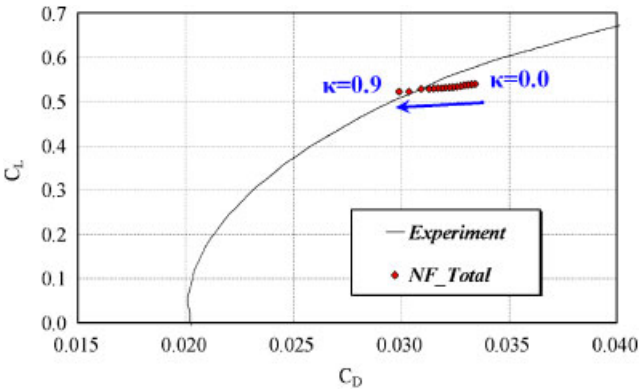

Figure 21. Near-field drag prediction for U-MUSCL scheme analysis.

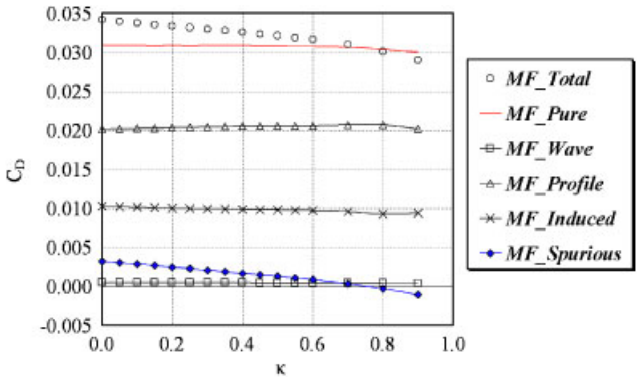

Figure 22. Drag decomposition results for U-MUSCL scheme analysis.

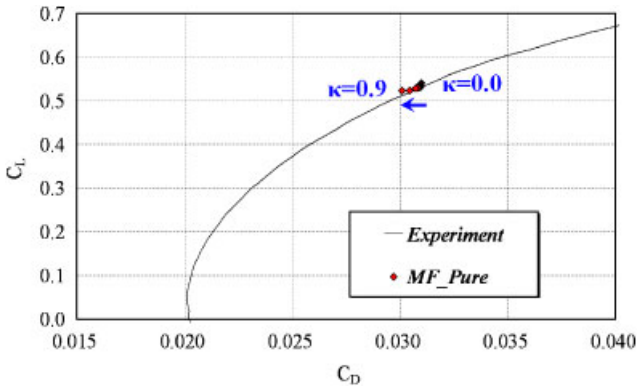

Figure 23. Pure drag prediction for U-MUSCL scheme analysis.

DOI: 10.1002/fld

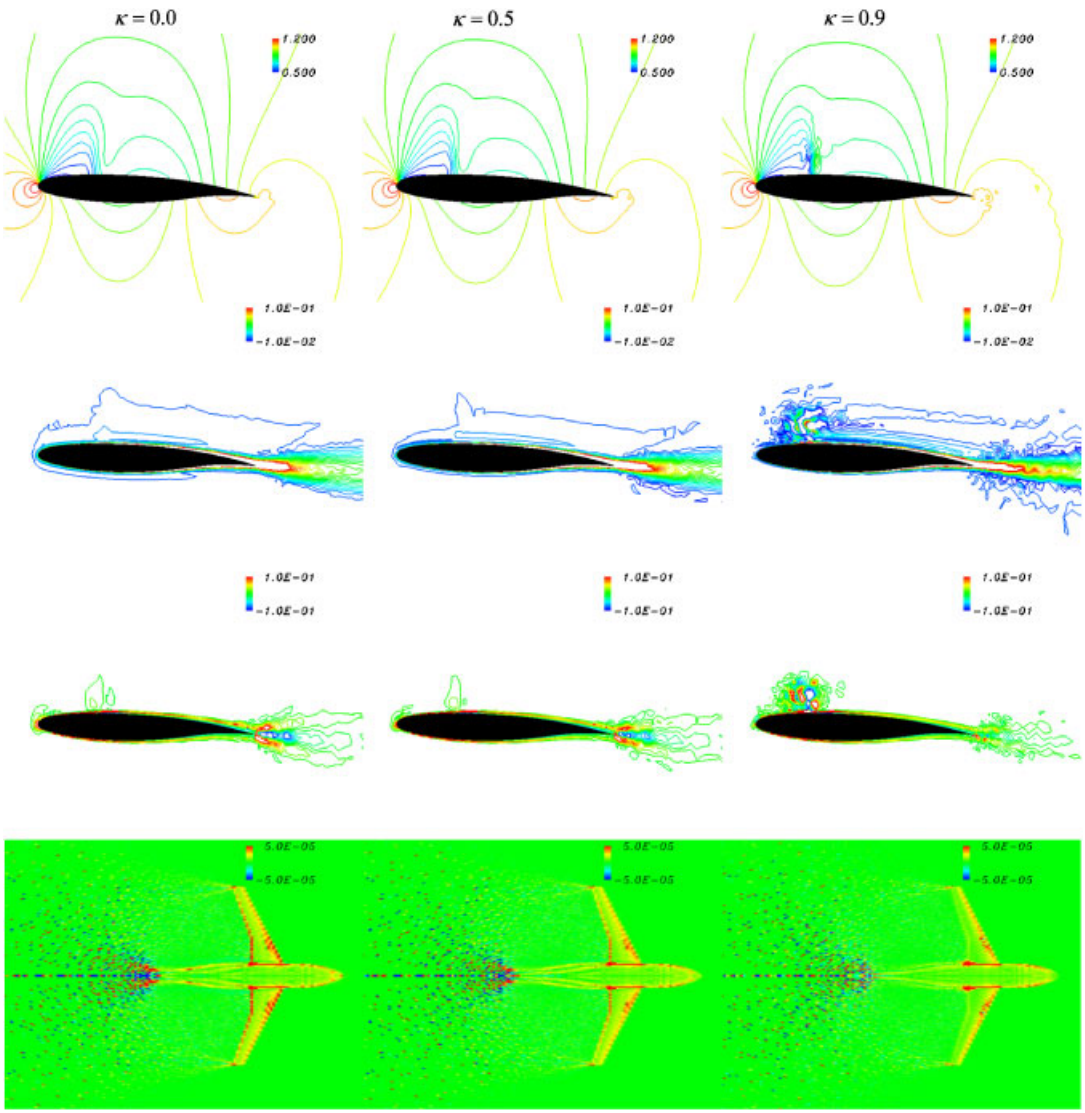

Figure 24. Flow-field visualization for U-MUSCL scheme analysis, from upper to lower: pressure, entropy variation, entropy drag distribution at 33% semi-span and entropy drag production map.

The number of mesh points was about 1 million. The transonic computations were then conduced, while changing the U-MUSCL parameter κ from 0 to 0.9 (unstable at 0.95).

In Figure 20, the C_p distributions for $\kappa = 0.0$, 0.5 and 0.9 at 41% semi-span section are compared with the experimental data. With the increase in κ, the shock wave was captured sharply. However, some oscillations around the shock wave and trailing edge were observed from the result for $\kappa = 0.9$, showing the limitation of stable computation. In Figure 21, the near-field drag prediction is plotted with the experimental data. As κ was increased from 0 to 0.9, a total drag reduction

DOI: 10.1002/fld

of about 35 cts and good agreement with the experimental data were confirmed. The total drag reduction was mainly due to the reduction of the pressure drag term. This result implied that the accuracy could be improved by using the U-MUSCL scheme and that the spurious drag could be reduced by increasing κ.

In Figure 22, the drag decomposition results are shown. The physical drag components were almost constant and independent of the parameter κ. Although the values fluctuated somewhat around $\kappa=0.8$–0.9, it was considered to be the effect of the computational instability. On the other hand, the spurious drag was reduced monotonically, and the value was negative at $\kappa>0.8$. The phenomenon of the negative spurious drag was reported in [12] and was caused by the negative entropy production at the border of the boundary layer. According to [12], this phenomenon appeared when central difference schemes were used for computations; the finding matched our results. In Figure 23, the mid-field pure drag prediction is plotted with the experimental data. The difference of pure drag between $0\leqslant\kappa\leqslant0.7$ was only about 3 cts and showed good agreement with the experimental data. This result showed that the physical drag components were predicted almost independent of the U-MUSCL parameter κ by using the drag decomposition method.

In Figure 24, the flow-field visualization at 33% semi-span and entropy drag production map are shown for the case of $\kappa=0.0$, 0.5 and 0.9. The reduction of spurious entropy drag at the leading edge and the reduction of the wake's diffusion can be observed with the increase in κ. The obscure shock wave on the upper surface at $\kappa=0.9$ showed the limitation of central difference schemes.

5. CONCLUSIONS

In this paper, the mid-field drag decomposition method was applied to unstructured mesh CFD results of the TAS-code. This method is able to decompose total drag into physical drag components to exclude the spurious drag component due to numerical diffusion and visualize the amount and generated positions of entropy drag in the flow field.

The mid-field drag prediction showed good agreement with the near-field one and provided meaningful results of drag decomposition. By the exclusion of the spurious drag component, pure drag showed good agreement with structured mesh results and experimental data. Thus, more accurate drag prediction was achieved with the mid-field method. In the mesh resolution analysis, only the spurious drag component was reduced with the increase in the mesh resolution. Hence, it was concluded that the physical drag components evaluated by the mid-field method were almost independent of the mesh resolution. Moreover, the reduction of spurious drag, which means the improvement in accuracy, was confirmed by using the U-MUSCL scheme.

These results could not have been obtained without using the mid-field drag decomposition method. For more accurate drag prediction, detailed analysis of drag reduction mechanisms and detailed data-mining of CFD results, the drag decomposition method will be an essential tool for aircraft designers and CFD researchers.

NOMENCLATURE

a	sonic speed
Body	aircraft surface
C_D	drag coefficient

DOI: 10.1002/fld

C_{L}	lift coefficient
C_p	pressure coefficient
D	drag force
$\mathbf{F}_{(\Delta s,\Delta H)}$	entropy and enthalpy drag vector
$\mathbf{F}_{\mathrm{ind}}$	induced drag vector
M	Mach number
$\mathbf{n}=(n_x,n_y,n_z)$	outward unit normal vector to a surface
P	pressure
Q	flow variables
$\mathbf{r}_{ij}$	vector between nodes i and j
R	gas constant
$\mathbf{S}_\infty$	closed boundary surface of $\mathbf{V}$
$\mathbf{u}=(u_x,u_y,u_z)$	velocity vector
$\mathbf{u}_\infty=(u_\infty,0,0)$	free stream velocity vector
$\mathbf{V}$	flow field around an aircraft
WA	wake plane normal to the free stream flow direction
$y+$	non-dimensional wall distance
Δ	perturbation term
ΔH	stagnation enthalpy variation
Δs	entropy variation
γ	specific heat ratio
κ	U-MUSCL parameter
μ_{l}	laminar viscosity coefficient
μ_t	eddy viscosity coefficient
ρ	density
$\overrightarrow{\tau}=(\boldsymbol{\tau}_x,\boldsymbol{\tau}_y,\boldsymbol{\tau}_z)^{\mathrm{T}}$	stress tensor
$\boldsymbol{\Psi}$	limiter

Subscripts

∞	free stream value
x,y,z	orthogonal coordinate system with the x-axis pointing to the free stream flow direction

ACKNOWLEDGEMENTS

The authors would like to thank Dr Kazuhiro Kusunose for his helpful advice. The authors also would like to thank Prof. Dimitri Mavriplis for providing the unstructured hybrid meshes of DLR-F6 geometry. This research was supported by a grant from the Japan Society for the Promotion of Science. The present computation was executed by using the NEC SX-7 in the Information Synergy Center at Tohoku University. The authors sincerely thank all the staff.

REFERENCES

1. Data available online at http://aaac.larc.nasa.gov/tsab/cfdlarc/aiaa-dpw/Workshop2/ (14/February/2007).
2. Data available online at http://aaac.larc.nasa.gov/tsab/cfdlarc/aiaa-dpw/ (14/February/2007).

DOI: 10.1002/fld

3. Hemsch MJ, Morrison JH. Statistical analysis of CFD solutions from 2nd drag prediction workshop. *AIAA Paper 2004-0556*, 2004.
4. Brodersen O, Rakowitz M, Amant S, Larrieu P, Destarac D, Sutcliffe M. *Airbus*, *ONERA*, *and DLR Results from the 2nd AIAA Drag Prediction Workshop*. *AIAA Paper 2004-0391*, 2004.
5. Laflin KR. *AIAA CFD Drag Prediction Workshop*: *An Overview*. *Proceedings of the 25th ICAS Congress*, *International Council of the Aeronautical Sciences*, Hamburg, 2006.
6. Kusunose K. A wake integration method for airplane drag prediction. *The 21st Century COE Program International COE of Flow Dynamics Lecture Series*, vol. 3, 2005.
7. Cummings RM, Giles MB, Shrinivas GN. Analysis of the elements of drag in three-dimensional viscous and inviscid flows. *AIAA Paper 96-2482-CP*, 1996.
8. Van Dam CP. Recent experience with different methods of drag prediction. *Progress in Aerospace Sciences* 1999; **35**(8):751–798.
9. Van Der Vooren J, Destarac D. Drag/thrust analysis of jet-propelled transonic transport aircraft: definition of physical drag components. *Aerospace Science and Technology* 2004; **8**(6):545–556.
10. Schmitt V, Destarac D. Recent progress in drag prediction and reduction for civil transport aircraft at ONERA. *AIAA Paper 98-0137*, 1998.
11. Paparone L, Tognaccini R. Computational fluid dynamics-based drag prediction and decomposition. *AIAA Journal* 2003; **41**(9):1647–1657.
12. Tognaccini R. Methods for drag decomposition. *von Karman Institute Lecture Series 2003-2*, 2003.
13. Yamazaki W, Matsushima K, Nakahashi K. Application of drag decomposition method to CFD computational results. *AIAA Paper 2005-4723*, 2005.
14. Yamazaki W, Matsushima K, Nakahashi K. Aerodynamic shape optimization based on drag decomposition. *AIAA Paper 2006-3332*, 2006.
15. Lovely D, Haimes R. Shock detection from computational fluid dynamics results. *AIAA Paper 99-3285*, 1999.
16. Nakahashi K, Ito Y, Togashi F. Some challenges of realistic flow simulations by unstructured grid CFD. *International Journal for Numerical Methods in Fluids* 2003; **43**(6–7):769–783.
17. Obayashi S, Guruswamy GP. Convergence acceleration of a Navier–Stokes solver for efficient static aeroelastic computations. *AIAA Journal* 1995; **33**(6):1134–1141.
18. Sharov D, Nakahashi K. Reordering of hybrid unstructured grids for lower–upper symmetric Gauss–Seidel computations. *AIAA Journal* 1998; **36**(3):484–486.
19. Spalart PR, Allmaras SR. A one-equation turbulence model for aerodynamic flows. *AIAA Paper 92-0439*, 1992.
20. Venkatakrishnan V. On the accuracy of limiters and convergence to steady state solutions. *AIAA Paper 93-0880*, 1993.
21. Burg COE. Higher order variable extrapolation for unstructured finite volume RANS flow solvers. *AIAA Paper 2005-4999*, 2005.
22. Ito Y, Nakahashi K. Surface triangulation for polygonal models based on CAD data. *International Journal for Numerical Methods in Fluids* 2002; **39**(1):75–96.
23. Sharov D, Nakahashi K. Hybrid prismatic/tetrahedral grid generation for viscous flow applications. *AIAA Journal* 1998; **36**(2):157–162.
24. Ito Y, Nakahashi K. Improvements in the reliability and quality of unstructured hybrid mesh generation. *International Journal for Numerical Methods in Fluids* 2004; **45**(1):79–108.
25. Data available online at http://www.grc.nasa.gov/WWW/wind/valid/m6wing/m6wing.html (14/February/2007).
26. Lee-Rausch EM, Frink NT, Mavriplis DJ, Rausch RD, Milholen WE. Transonic drag prediction on a DLR-F6 transport configuration using unstructured grid solvers. *AIAA Paper 2004-0554*, 2004.

DOI: 10.1002/fld